International Journal of Hydrogen Energy 68 (2024) 360–373

Contents lists available at ScienceDirect

International Journal of Hydrogen Energy

journal homepage: www.elsevier.com/locate/he

# Multi-objective optimization of the hydrogen fuel production of a solar-based cobalt-chlorine (Co–Cl) thermochemical cycle with grey relational analysis

Ramazan Çakıroğlu *, Oğuz Kaan Çinici, Şulenur Asal, Adem Acır

*Gazi University, Faculty of Technology, Department of Energy Systems Engineering, 06500, Ankara, Türkiye*

ARTICLE INFO

Handling Editor: Prof B Shabani

*Keywords:*
Solar energy
Grey relational analysis
ANOVA
Hydrogen production
Cobalt chlorine (Co–Cl) cycle

ABSTRACT

In this paper, multi-objective optimization of the hydrogen production ($\dot{m}_{H_2}$) of a solar-based cobalt-chlorine (Co–Cl) thermochemical cycle with grey relational analysis (GRA) has been performed. Monthly total irradiance averages (A), wind velocity (B), receiver height (C), receiver radius (D) and number of heliostats (E) are considered to achieve the highest the useful energy absorbed by the solar receiver ($\dot{Q}_{abs}$), efficiency of the receiver ($\eta_{rec}$), the overall efficiency of the system ($\eta_{overall}$) and hydrogen production ($\dot{m}_{H_2}$). Orthogonal experimental design is planned according to $L_{18}$ orthogonal array created by Taguchi method. The percent contribution rates (PCR) on the $\dot{Q}_{abs}$, $\eta_{rec}$, $\eta_{overall}$ and $\dot{m}_{H_2}$ are determined with the help of ANOVA analysis. The optimal parameters are identified as monthly total irradiance average of 143.8 kW h ($A_3$), wind velocity of 5 m/s ($B_2$), receiver height of 8 m ($C_1$), receiver radius of 3 m ($D_1$) and number of heliostats of 850 ($E_3$), respectively. The highest $\dot{Q}_{abs}$, $\eta_{rec}$, $\eta_{overall}$ and $\dot{m}_{H_2}$ values corresponding to $A_3B_2C_1D_1E_3$ are obtained as 50.2 GW; 64.1%; 22.2% and 122.59 (tons/month), respectively. The PCR of the A, B, C, D and E parameters influencing the f-factor are determined to be 12.6 %, 1.92 %, 0.48 %, 15.03 %, and 53.20 %, respectively. Also, empirical equations are developed with regression analysis (RA) to estimate the $\dot{Q}_{abs}$, $\eta_{rec}$, $\eta_{overall}$, $\dot{m}_{H_2}$ values. The statistical coefficients ($R^2$-value) for training and testing data's are determined in the range of 0.771167–0.99608 for $\dot{Q}_{abs}$, $\eta_{rec}$, $\eta_{overall}$ and $\dot{m}_{H_2}$, respectively.

## 1. Introduction

While the world population is increasing and technology is developing, the energy requirement is increasing day by day. Most of the current energy consumption is provided by fossil fuels, which are limited reserves. As a result of the combustion of fossil fuels, environmentally detrimental gases such as $CO_2$, $SO_x$, and $NO_x$ are released. These gases cause ozone layer depletion and global warming. For this reason, researchers have directed the search for environmentally friendly alternative fuels instead of traditional fossil fuels. Hydrogen is one of them for a clean and sustainable energy future [1,2]. Hydrogen plays an important role among sustainable energy options due to its ability to reduce greenhouse gas emissions [3]. Also, hydrogen production from fossil fuels tends to result in substantial carbon emissions, which is why renewable energy-based approaches for hydrogen production are gaining increasing attention [4]. There are a lot of studies in the literature on hydrogen production using renewable energy sources. Demir and Dincer [5] have been proposed and analyzed thermodynamically for electricity and hydrogen ($H_2$) production via a solar heliostat-based hybrid system integrated with NaOH-PCM. The total hydrogen production per day and electrical energy output of the hybrid system was 129.9 kg and 50.6 GJ/day, respectively. Behzadi et al. [6] investigated an innovative multi-generation plant, driven by the central receiver based concentrated solar systems. An innovative approach for reducing greenhouse gas emissions with by using vanadium chlorine thermochemical cycle have been presented. The produced hydrogen rate increased more than 500 % increment with by rising the solar radiation and the emission $CO_2$ reduced from 0.129 kg/kWh to 0.026 kg/kWh. Ratlamwala et al. [7] performed energy, exergy and optimization an integrated system encompassing a heliostat field, a steam cycle, an organic Rankine cycle, and an electrolyzer. As they increased the heliostat field area from 8000 $m^2$ to 50000 $m^2$, they observed a

* Corresponding author.
*E-mail address:* rcakiroglu@gazi.edu.tr (R. Çakıroğlu).

https://doi.org/10.1016/j.ijhydene.2024.04.219
Received 25 January 2024; Received in revised form 8 April 2024; Accepted 19 April 2024
0360-3199/© 2024 Hydrogen Energy Publications LLC. Published by Elsevier Ltd. All rights reserved.

corresponding rise in the mass flow rate of hydrogen production, which went from 0.006 kg/s to 0.063 kg/s. The maximum energy and exergy efficiencies and produced hydrogen rate was obtained as 18.74%, 39.55% and 1571 L/s, respectively. Musharavati et al. [8] investigated a solar-based energy plant which has an NH3–LiNO3 operated refrigeration system, an organic Rankine cycle and PEM electrolyzer. They observed a substantial 150% increase in hydrogen production when utilizing n-octane as the working fluid under solar radiation of 800 W/m$^2$. Alirahmi et al. [9] proposed an efficient and environmentally friendly hybrid energy production/storage system consisting of compressed air energy storage, heliostat-driven Brayton cycle and hydrogen production unit, which minimizes the pollutant emissions of compressed air energy storage technology. Izadi et al. [10] investigated a trigeneration system which has is composed of solar boosted gas turbine, desalination unit, LiBr/$H_2O$ absorption chiller, TEGs, and hydrogen production unit integrated with solar heliostat towers. It is observed that fuel consumption is decreased, and exergy efficiency is increased nearly 2.92% by using a solar heliostat system. Özdemir and Genç [11] performed energy and exergy analysis is performed for solar based hydrogen production via Mg–Cl, $H_2SO_4$, and UT-3 cycles. The highest exergy efficiency with Mg–Cl thermochemical and recompression S–$CO_2$ Brayton power cycles was obtained as 27%. El-Emam and Dincer [12] analyzed solar heliostat based integrated system which has aimed cooling, hot water, producing electric power, fresh water and hydrogen production. It concluded that amount of electric power, hydrogen and fresh water were computed as 4 MW, 1.25 kg/h and 90 kg/s, respectively. Hai et al. [13] presented a novel power generation plant integrated with an electrolyzer based on supercritical Closed Brayton Cycle (CBC) driven by solar heliostat field for green hydrogen production. The presented combined cycle has 15.8% higher produced hydrogen rate than the CBC-based system. Furthermore, hydrogen can be produced via many thermochemical cycles, including copper-chlorine (Cu–Cl), sulfur-iodine (S–I), iron-chlorine (Fe–Cl), magnesium-chlorine (Mg–Cl), and cobalt-chlorine (Co–Cl) cycles as well as plant integrated with an electrolyzer. Within the scope of this study, Co–Cl cycle is chosen to investigate hydrogen production potential via solar heliostat system. The Co–Cl cycle is one of the suggested a novel hydrogen production cycles by Canavesio et al. [14]. When the literature studies are examined rather than other processes, it is seen that there are a few studies about Co–Cl cycle. Asal and Acır [15] investigated to hydrogen production potential of the Co–Cl cycle using the Laser Inertial Fission-Fusion Engine (LIFE). In the study, hydrogen production cycle was examined via Shomate equation and two different type of nuclear fuel were used to assess the effect on hydrogen production amount. Oruc and Dincer [16] made an exergy analysis of Co–Cl cycle using Aspen Plus software. They investigated each reaction kinetically under numerous temperature and pressure values. Asal and Acır [17] compared three thermochemical cycle; Cu–Cl, S–I, and Co–Cl cycles to examine the hydrogen production potential of the LIFE engine. Since the literature studies on Co–Cl cycle were presented related to nuclear energy or exergy analysis of the cycle up to the present, the solar-based Co–Cl is assessed in this proposed study as novelty for hydrogen production.

The optimization techniques such as Taguchi, Grey relation analysis and response surface method are applied to provide clear recommendation for the best design parameter in the proposed systems. With the Grey relation optimization method, the number of experiments is significantly reduced, and time and cost are saved. Especially for the GRA optimization technique helps researchers to determine the optimum experiment variables without spending more time [18,19].

Differing from the Co–Cl cycle studies in the literature, proposed system in this paper aims to investigate the optimal hydrogen production potential of a solar-bases Co–Cl cycle with by using grey relational analysis (GRA). The effect of the monthly total irradiance averages (A), wind velocity (B), receiver height (C), receiver radius (D) and number of heliostats (E) on the $\dot{Q}_{abs}$, $\eta_{rec}$, $\eta_{overall}$, $\dot{m}_{H_2}$ of the solar-based have been optimized. The experimental design with five factors and six levels of the $L_{18}$ orthogonal array to determine optimal design levels have been performed. Also, The percent contribution rates (PCR) on the $\dot{Q}_{abs}$, $\eta_{rec}$, $\eta_{overall}$ and $\dot{m}_{H_2}$ are determined with the help of ANOVA analysis. Empirical equations have been developed with regression analysis (RA) depending on the determined operation parameters. Also, monthly hydrogen production ($\dot{m}_{H_2}$) at optimum design, parameters were computed and compared.

## 2. Problem description

The solar-based hydrogen production system flow chart is shown in Fig. 1. The solar-based Co–Cl is assessed in this proposed study as novelty for hydrogen production. The solar-driven hydrogen production system comprises four key components: a solar heliostat field, a central receiver, a phase change material (PCM) unit, and a hydrogen production facility. In the heliostat unit, sunlight is captured and focused by the solar heliostat onto the central receiver. The thermal energy from the receiver is absorbed and stored using the PCM. Subsequently, this stored thermal energy is directed to the hydrogen production facility, which generates hydrogen through four distinct thermochemical reactions. Importantly, in this study, it is assumed that all the thermal energy absorbed by the PCM is exclusively channeled to the hydrogen production facility, bypassing the gas turbine for electricity generation. In this system, the analyses were calculated for six months of average solar flux values for Türkiye, and flux values are given in Table 1 [20]. Additionally, in addition to solar flux values, an experimental design was made for three different wind speeds: receiver heights, receiver radius, and solar heliostat numbers. Thermodynamic analyses and hydrogen production have been evaluated according to the experimental designs. All required parameter's values for a solar system have been given in Table 2 [21–30]. The solar-based Co–Cl cycle assessed in this proposed study as novelty thermochemical cycle for hydrogen production [15,31], and these cycles have been selected for this study. The effect of the parameters planned in the experimental design to determine the optimum design parameters have been investigated on the $\dot{Q}_{abs}$, $\eta_{rec}$, $\eta_{overall}$, $\dot{m}_{H_2}$.

## 3. Energy analysis for the overall system

Thermodynamic analyses of this solar-based hydrogen production system was investigated for different solar flux and heliostat area values. The energy analysis of the solar-based hydrogen production system was analyzed by making the below assumptions [21,26].

- All pressure drops in the system are neglected.
- The reference ambient conditions are utilized as 25 °C environment temperature ($T_0$) and 100 kPa pressure ($P_0$).
- The kinetic and potential energy have been ignored.
- All the heat absorbed by the PCM is sent to the hydrogen production facility.

### 3.1. Solar system (heliostat and central receiver)

The solar system comprises two main components: the heliostat field and the central receiver. The sunlight collected by the heliostat is redirected towards the central receiver, where it is concentrated. The concentrated sunlight's heat in the central receiver is then stored in the phase change material (PCM), fulfilling the heat requirements for hydrogen production. The total incoming solar flux on the heliostat field is determined using Eq. (1) [21,25–28];

$$\dot{Q}_{field} = I \times A_{field} \tag{1}$$

In this context, $A_{field}$ denotes the overall area of the heliostat field, and $I$

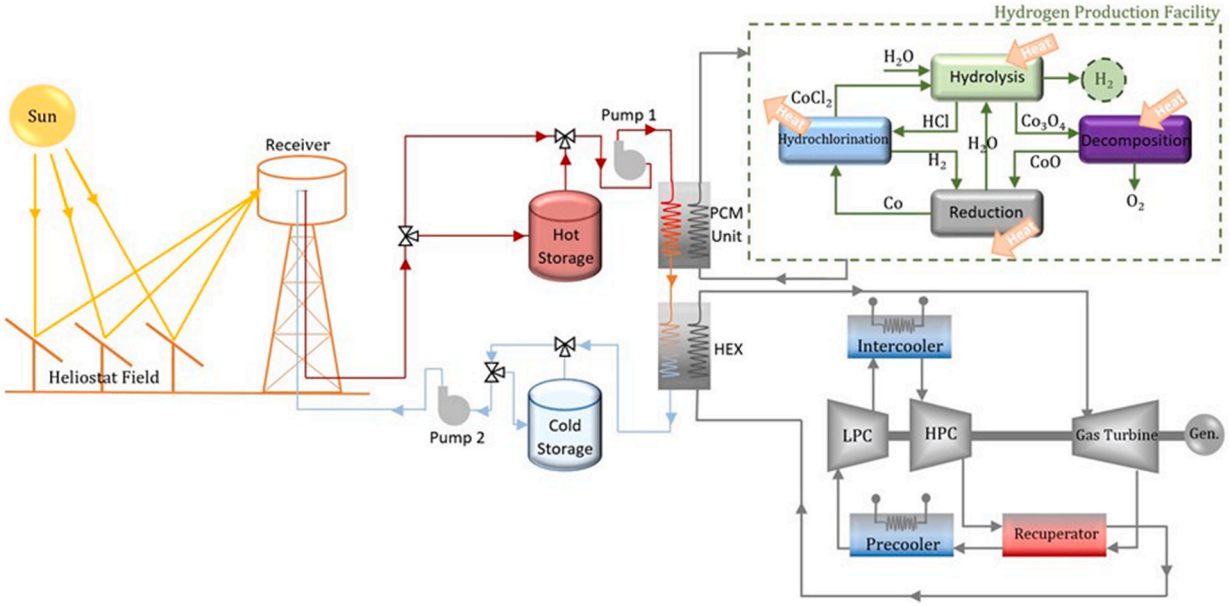



**Fig. 1.** Flow diagram of solar based hydrogen production system via Co–Cl cycle [15,21,24]
(LPC: Low pressure compressor, HPC: High pressure compressor, Gen.: Generator).

**Table 1**
Solar irradiation values for 6-months of Türkiye [20].

| Months | Average Monthly Irradiance (kWh) | Monthly Average Daily Sunbathing Time (h) |
|---|---|---|
| April | 143.8 | 6 |
| May | 203.3 | 9.1 |
| June | 204.4 | 9.2 |
| July | 211.4 | 10.1 |
| August | 188.7 | 9.5 |
| September | 143.9 | 8 |

**Table 2**
Required parameters for solar heliostat [21–31].

| Subsystem | Parameters | Value |
|---|---|---|
| **Solar Heliostat** | Field of a heliostat | 121 $m^2$ |
| | Efficiency, $\eta_h$ | 0.71 |
| | Concentration ratio, $C$ | 1000 |
| **Central Receiver** | Aperture field, $A_{rec,ape}$ | 0.121 $m^2$ |
| | Receiver surface area, $A_{rec,surf}$ | 140.19 $m^2$ |
| | Surface temperature, $T_{rec,surf}$ | 1000 °C |
| | Tube diameter | 0.019 $m$ |
| | Tube thickness | 0.00165 $m$ |
| | Tube thermal conductivity | 23.9 W/mK |
| | Tube insulation thickness | 0.07 $m$ |
| | Tube insulation thermal conductivity | 0.05 W/mK |
| | View factor, $F_r$ | 0.8 |
| | Emissivity, $\varepsilon_w$ | 0.8 |
| | Reflectivity, $\rho$ | 0.04 |
| | Wind velocity | 5 m/s |
| **Phase Change Material (PCM)** | PCM compound | $Na_2CO_3$ - $BaCo_3$ – MgO |
| | PCM density | 2600 $kg/m^3$ |
| | PCM enthalpy of fusion | 415.4 kJ/kg |

represents the solar flux expressed in units of $W/m^2$. We compute the quantity of thermal energy that the heliostat field directs towards the receiver in the following manner: [21,25–28];

$$\dot{Q}_{rec} = \eta_h \times \dot{Q}_{field} \tag{2}$$

where, $\eta_h$ is the heliostat's efficiency, and this value is given in Table 2.

The total absorbed thermal energy for the solar receiver is defined as [21,25–28];

$$\dot{Q}_{rec} = \dot{Q}_{abs} + \dot{Q}_{total,loss} \tag{3}$$

where, $\dot{Q}_{abs}$ is the useful energy absorbed by the solar receiver and $\dot{Q}_{total,loss}$ represents the thermal energy losses in the receiver. $\dot{Q}_{total,loss}$ specifies the total thermal power losses, which are formulated as [27,28,30]:

$$\dot{Q}_{tatal,loss} = \dot{Q}_{cond} + \dot{Q}_{ref} + \dot{Q}_{rad} + \dot{Q}_{conv} \tag{4}$$

where it is seen that there is heat transfer from the receiver by heat transfer mechanisms, conduction ($\dot{Q}_{cond}$), reflection ($\dot{Q}_{ref}$), radiation ($\dot{Q}_{rad}$), forced and natural convection ($\dot{Q}_{conv}$).

Conductive heat loss occurs in three distinct areas: heat transfer through conduction from the insulation layer, the support structure, and the air convection between the insulation layer and the receiving panel. Therefore, the conductive heat losses stemming from the support structure and the air convection between the insulating layer and the receiving panel were negligible and can be disregarded. Consequently, conduction heat loss is calculated using Eq. (5) provided in Refs. [27,28,30].

$$\dot{Q}_{cond} = \frac{\left(T_{rec,surf} - T_0\right) A_{field}}{\left(\frac{\delta_{insu}}{\lambda_{insu}} + \frac{1}{h_{air,0}}\right) C \times F_r} \tag{5}$$

where, $\delta_{insu}$ is insulation thickness, $\lambda_{insu}$ is the thermal conductivity of insulation, $C$ is the concentration ratio, obtained as the ratio of the heliostat area to the aperture area of the receiver, Eq. (6), and $F_r$ is the view factor and is defined as the ratio of the aperture area of the receiver to the receiver surface area, Eq. (7) [21–25]:

$$C = \frac{A_{field}}{A_{rec,ape}} \tag{6}$$

$F_r = \frac{A_{rec,ape}}{A_{rec,surf}}$ (7) As can be seen in Eq. (8), the aperture area of the receiver is equal to the width of the receiver aperture multiplied by the receiver height. Also, the width of the receiver opening can be considered half the receiver height as given Eq. (8) [29].

$$A_{rec,ape} = H \times W, W = 0.5 \times H \tag{8}$$

The reflection heat loss occurs at the surface of the receiver and is calculated as given Ref. [21,25,27,29,30].

$$\dot{Q}_{ref} = \rho \times \dot{Q}_{rec} \times F_r \tag{9}$$

Here, $\rho$ is the reflectivity, which is given in Table 2. The radiative heat loss depends on the receiving surface and ambient temperature and is calculated with Eq. (10) as presented Ref. [21,25,27,29,30].

$$\dot{Q}_{rad} = \frac{\varepsilon_{avg}\sigma\left(T_{rec,sur}^4 - T_a^4\right)A_{field}}{C} \tag{10}$$

where $\sigma$ is Stefan–Boltzmann constant ($5.67 \times 10^{-8}\ W/m^2K^4$) and $\varepsilon_{avg}$ is emissivity defined with Eq. (11) [21,25,27,29,30].

$$\varepsilon_{avg} = \frac{\varepsilon_w}{\varepsilon_w + (1-\varepsilon_w)F_r} \tag{11}$$

The convective heat loss occurs in two ways as forced convection ($\dot{Q}_{conv,fc}$) and natural convection ($\dot{Q}_{conv,nc}$) as given Ref. [21,25,27,29,30].

$$\dot{Q}_{conv} = \dot{Q}_{conv,fc} + \dot{Q}_{conv,nc} \tag{12}$$

The heat dissipation due to forced convection at the receiver was assumed to be analogous to the forced convection loss experienced by a flat plate, as described in Ref. [30]. This can be quantified using Eq. (13) provided in Refs. [21,25,27,29,30].

$$\dot{Q}_{conv,fc} = h_{fc}\left(T_{rec,surf} - T_a\right)A_{rec,surf} \tag{13}$$

In this context, the "film temperature" is defined as the average temperature between the surface of the receiver and the surrounding air. The forced heat transfer coefficient required for calculations can be determined using the abovementioned Eq. (14) as presented Ref. [21,25,27,29,30].

$$h_{fc} = \frac{Nu_{fc} \times k_{air}}{H} \tag{14}$$

$$Nu_{fc} = 0.0287 Re_{fc}^{0.8} \times Pr_{air}^{1/3} \tag{15}$$

Natural convection heat loss was treated analogous to a flat plate, following the approach that was proposed by Siebers and Kraabe [30]. The calculation of the forced heat transfer coefficient can be accomplished using Eqs. 16 and 17 found in Refs. [21,24,26–30].

$$\dot{Q}_{conv,nc} = h_{nc}\left(T_{rec,surf} - T_0\right)A_{rec,surf} \tag{16}$$

$$h_{nc} = 0.81\left(T_{rec,surf} - T_0\right)^{0.426} \tag{17}$$

### 3.2. PCM unit

In this solar heliostat-based hydrogen production system, the heat generated by the solar receiver is stored within a phase change material (PCM). This stored thermal energy is subsequently utilized to provide the necessary heat for hydrogen production. Specifically, the PCM employed in this system is composed of $Na_2CO_3$, $BaCO_3$, and MgO, with a high melting temperature of 850 °C. This high melting point is crucial to ensure that it can supply the requisite thermal energy for hydrogen production, as outlined in Ref. [23].

The amount of thermal energy absorbed by the PCM relies on two key factors: the mass flow rate of the PCM ($\dot{m}_{pcm}$) and the heat of fusion of the PCM ($\Delta H_{pcm}$), as described in Eq. (18) from Ref. [23].

$$\dot{Q}_{abs} = \dot{m}_{pcm}\Delta H_{pcm} \tag{18}$$

According to absorbed thermal energy and the receiver's thermal energy values, the efficiency of the receiver is calculated with Eq. (19) [2,25].

$$\eta_{rec} = \frac{\dot{Q}_{abs}}{\dot{Q}_{rec}} \tag{19}$$

### 3.3. Hydrogen production facility via cobalt-chlorine (Co–Cl) cycle

The Co–Cl thermochemical cycle, a novel method, consists of four main reactions. Cycle reactions occur at 700 °C [14], and the cycle schematic representation is given in Fig. 2 [33].

Hydrolysis of cobalt chloride ($CoCl_2$):

$$3CoCl_{2(s)} + 4H_2O_{(g)} \rightarrow Co_3O_{4\ (s)} + 6HCl_{(g)} + H_{2(g)} \tag{20}$$

Thermal decomposition of tricobalt tetraoxide ($Co_3O_4$):

$$Co_3O_{4(s)} \rightarrow 3CoO_{(s)} + 0.5O_{2(g)} \tag{21}$$

Reduction of cobalt oxide (CoO):

$$3CoO_{(s)} + 3H_{2(g)} \rightarrow 3Co_{(s)} + 3H_2O_{(g)} \tag{22}$$

Hydrochlorination of metallic cobalt (Co):

$$3Co_{(s)} + 6HCl_{(g)} \rightarrow 3CoCl_{2(s)} + 3H_{2(g)} \tag{23}$$

The Co–Cl cycle is one of the water-splitting methods. It consists two endothermic and two exothermic reactions. The first reaction is hydrolysis reaction, solid phased $CoCl_2$ and superheated steam react and solid phased $Co_3O_4$ and gas phased HCl and H2 occur. $Co_3O_4$ decompose in the second reactor to CoO and $O_2$. CoO is sent to the reduction reactor and $O_2$ is obtained as a product. In the third reactor, CoO and $H_2$ that comes from hydrochlorinaiton reaction react to occur Co and $H_2O$. While Co goes to the hydrochlorination reactor, $H_2O$ is used as a reactant in the first reactor. Ultimate reaction is the hydrochlorination reaction. Here, Co and HCl that comes from the first reaction react and at the end of the reaction, $CoCl_2$ and $H_2$ occur. These outputs are utilized again in the first and third reactors separately [14,15].

The mass flow rate of the generated hydrogen (kg/s) has been determined using mass ratio balance equations, specifically, Eqs. 24–26. The comprehensive explanations and further details regarding these mass flow ratio balance equations can be found in Refs. [34,35].

$$\sum \dot{m}_{in} = \sum \dot{m}_{out} \tag{24}$$

$$\dot{m}_x = \frac{\dot{Q}_{abs}\varphi}{q_{tot}} \tag{25}$$

$$\dot{m}_y = \dot{m}_x \frac{u_y}{u_x}\eta \tag{26}$$

In these equations, $m$ represents the mass flow rate, $u$ signifies the molar mass of the compounds, and $\eta$ corresponds to the efficiency of reactions, which is assumed to be 0.90 in this context. Additionally, $q_{tot}$ represents the total energy value. The indices "in" and "out" are used to differentiate between the reactants and products involved in each chemical reaction, while " $x$" and " $y$ " serve as illustrative placeholders for specific elements within these reactions. Additionally, $\varphi$ is the hydrogen production fraction, and this value is %100. In this study, calculations were made by assuming that all the heat absorbed by the PCM is sent to the hydrogen production facility, so the electrical power fraction (1-$\varphi$) is zero. The total energy value for the Co–Cl thermochemical cycle has been assessed by using the Shomate equation [17,34,36]

The general energy rate balance Eq. (27) [36]:

$$\sum \dot{Q}_{in} + \sum \dot{W}_{in} + \sum \dot{m}_{in}\left(h_{in} + \frac{V_{in}^2}{2} + gZ_{in}\right) = \sum \dot{Q}_{out} + \sum \dot{W}_{out} + \sum \dot{m}_{out}\left(h_{out} + \frac{V_{out}^2}{2} + gZ_{out}\right) \tag{27}$$

Shomate equations is given in Eqs. 28 and 29 [17,34,36].

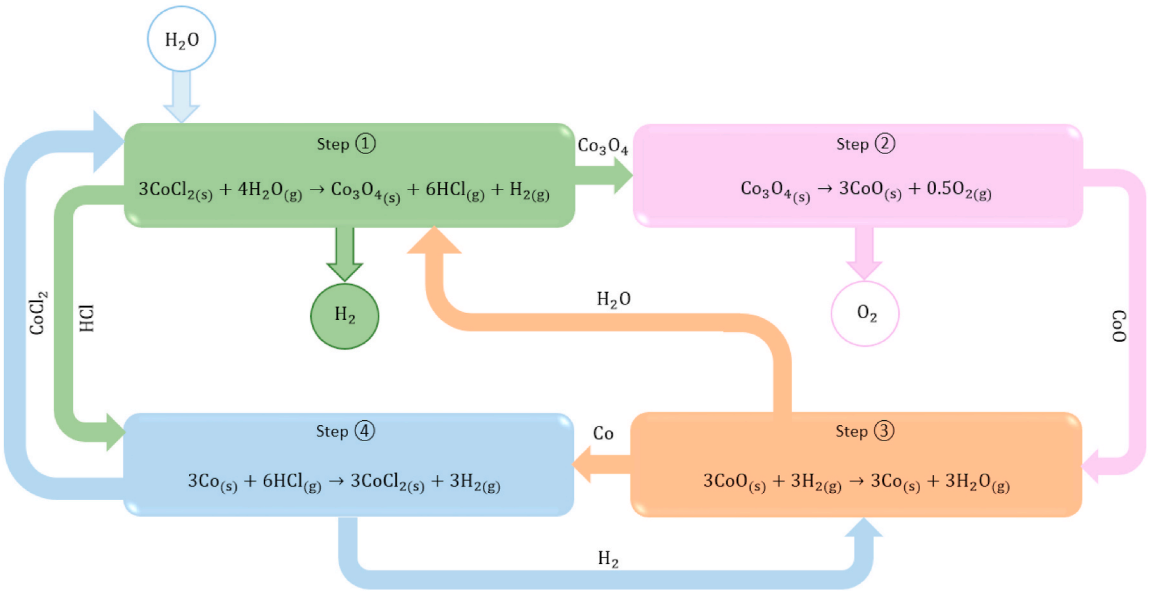



**Fig. 2.** Schematic representation of Co–Cl thermochemical cycle [15,17].

**Table 3**
Co–Cl cycle needed parameters for Shomate equation [15].

| Cycle | Compound | $\overline{h}_f^o$ (kJ/mol) | X | Y | Z | W | Q | H | G |
|---|---|---|---|---|---|---|---|---|---|
| Co–Cl cycle | $CoCl_2$ (s) | −312.55 | 79.30939 | 14.28782 | −6.293698 | 1.317864 | −0.402808 | −338.1274 | −312.5452 |
| | $H_2O$ (g) | −241.83 | 30.092 | 6.832514 | 6.793435 | −2.53448 | 0.082139 | −250.881 | −241.8264 |
| | $Co_3O_4$ (s) | −910.02 | 177.0953 | −100.4361 | 185.7792 | −49.4861 | −3.483951 | −971.5415 | −910.02 |
| | HCl (g) | −92.31 | 32.12392 | −13.45805 | 19.86852 | −6.853936 | −0.049672 | −101.6206 | −92.31201 |
| | $H_2$ (g) | 0 | 33.066178 | −11.363417 | 11.432816 | −2.772874 | −0.158558 | −9.980797 | 0 |
| | CoO (s) | −237.74 | 43.65 | 22.38373 | −16.89386 | 6.556161 | 0.532263 | −249.8643 | −237.7353 |
| | $O_2$ (g) | 0 | 30.0235 | 8.772972 | −3.988133 | 0.788313 | −0.741599 | −11.32468 | 0 |
| | Co (s) | 0 | −204.576 | 515.582 | −421.55 | 129.558 | 17.9267 | 94.6155 | 0 |

$$\dot{Q} = \sum n_{out}\left(\overline{h}_f^o + \overline{h} - \overline{h}_0\right)_{out} - \sum n_{in}\left(\overline{h}_f^o + \overline{h} - \overline{h}_0\right)_{in} \tag{28}$$

$$\overline{h}(T) - \overline{h}_0 = AT + B\frac{T^2}{2} + C\frac{T^3}{3} + D\frac{T^4}{4} - \frac{E}{T} + F - H \tag{29}$$

In this context, $\dot{E}$ represents the total energy transfer measured in kilowatts (kW). $\dot{Q}$ signifies the energy transfer due to heat, also measured in kilowatts (kW), while " $\dot{W}$" stands for the energy transfer through mechanical work, also in kilowatts (kW). The symbols $\overline{h}_f^o$ , $\overline{h}(T)$ and $\overline{h}_0$ pertain to enthalpy values: $\overline{h}_f^o$ represents the enthalpy of formation in kJ per mole (kJ/mol), $\overline{h}(T)$ denotes the sensible enthalpy at a particular state, also in kJ/mol, and $\overline{h}_0$ stands for the standard sensible enthalpy at 25 °C and 1 atm, measured in kJ/mol. The variable $T$ is equal to 1/1000 of the specified temperature in Kelvin, and the constants "X," "Y," "Z," "W," "Q," "H," and "G," are cited from Ref. [36] and tabulated in Table 3 [17], are used in calculations.

Finally, the overall efficiency of the system is calculated with Eq. (30) [37].

$$\eta_{overall} = \frac{\dot{m}_{H_2} \times HHV}{\dot{Q}_{field}} \tag{30}$$

### 3.4. Taguchi-based grey relational analysis (GRA)

GRA is a powerful tool for analyzing the dynamic properties of complex and abstract problems and transforming multi-objective optimization problems into single-objective problems. One of the advantages of GRA is that it deals with both quantitative and qualitative data, making it a versatile tool that can be used in many situations. GRA is an easy to understand and apply method for situations where time is limited or more complex methods are not required [38]. Simplicity of use, minimum data requirement and regression analysis are among the advantages of GRA. Also, the most influential factors affecting the response variables through GRA are resulted in a single parametric combination that improves the overall process [39].

This section aims to optimize the operating parameters affecting the

**Table 4**
Factors and levels used in the experiments.

| Symbol | Parameters | Levels | | | | | |
|---|---|---|---|---|---|---|---|
| | | 1 | 2 | 3 | 4 | 5 | 6 |
| A | Monthly total irradiance average (kWh) [20] | 143.8 | 203.3 | 204.4 | 211.4 | 188.7 | 143.9 |
| B | Wind velocity (m/s) [22,23] | 4 | 5 | 6 | | | |
| C | Receiver height, H (m) [25,31,32] | 8 | 10 | 12 | | | |
| D | Receiver radius, R (m) [25] | 3 | 4 | 5 | | | |
| E | Number of heliostats [23,24] | 450 | 650 | 850 | | | |

**Table 5**
Experimental design using $L_{18}$ orthogonal array.

| Exp. no. | A Monthly total irradiance average (W) | B Wind velocity (m/s) | C Receiver height, H (m) | D Receiver radius, R (m) | E Number of heliostats |
|---|---|---|---|---|---|
| **1** | 143.8 | 4 | 8 | 3 | 450 |
| **2** | 143.8 | 5 | 10 | 4 | 650 |
| **3** | 143.8 | 6 | 12 | 5 | 850 |
| **4** | 203.3 | 4 | 8 | 4 | 650 |
| **5** | 203.3 | 5 | 10 | 5 | 850 |
| **6** | 203.3 | 6 | 12 | 3 | 450 |
| **7** | 204.4 | 4 | 10 | 3 | 850 |
| **8** | 204.4 | 5 | 12 | 4 | 450 |
| **9** | 204.4 | 6 | 8 | 5 | 650 |
| **10** | 211.4 | 4 | 12 | 5 | 650 |
| **11** | 211.4 | 5 | 8 | 3 | 850 |
| **12** | 211.4 | 6 | 10 | 4 | 450 |
| **13** | 188.7 | 4 | 10 | 5 | 450 |
| **14** | 188.7 | 5 | 12 | 3 | 650 |
| **15** | 188.7 | 6 | 8 | 4 | 850 |
| **16** | 143.9 | 4 | 12 | 4 | 850 |
| **17** | 143.9 | 5 | 8 | 5 | 450 |
| **18** | 143.9 | 6 | 10 | 3 | 650 |

amount of hydrogen produced by the solar-based cobalt-chlorine (Co–Cl) thermochemical cycle using the GRA method. Experimental design (DOE) factors and levels with Taguchi-based GRA have been determined as monthly total irradiance average, wind velocity, receiver height, receiver radius, and number of heliostats, as presented in Table 4. The experimental design with five factors and six levels have been determined by using Minitab software. The experimental design has been designed as a Taguchi $L_{18}$ orthogonal array as given in Table 5. Taguchi $L_{18}$ orthogonal array has been utilized to decrease of the experiment test. The algorithm structure and equations required for the optimum experimental design with the GRA method have been presented in Fig. 3. The results obtained from the experiments are normalized between zero (0) and one (1) in GRA, depending on the experimental design. The normalization of the $\dot{Q}_{abs}$, $\eta_{rec}$, $\eta_{overall}$, $\dot{m}_{H_2}$ have been conducted in the case of the "higher the better" process according to the equation given in Fig. 4.

## 4. Result and discussions

### 4.1. Grey relational analysis of optimum parameters

The parameters where one factor has six variables, and four factors have three variables are given in Table 4. Accordingly, the Taguchi $L_{18}$ (6^1–3^4) orthogonal experimental design is presented in Table 5. Table 6 shows the results of the grey relation analysis, which consists of the $\dot{Q}_{abs}$, $\eta_{rec}$, $\eta_{overall}$, $\dot{m}_{H_2}$ obtained depending on the variable sequence and number of experiments.

For the $L_{18}$ experiment design, the $\dot{Q}_{abs}$, $\eta_{rec}$, $\eta_{overall}$, $\dot{m}_{H_2}$ are required to be at the best level for maximum performance. Therefore, grey relational coefficients have been calculated for all experiments with the help of the equation given in Fig. 3, and the "higher the better" normalization sequence approach has been used. All calculated results are normalized and presented in Table 6. As presented in Table 6 and Fig. 5, the highest grade has been obtained as for experiment 11.

Firstly, the average of the sum of the same grade values was examined for each parameter, and the overall grey relational grade was obtained. This process was repeated for each parameter at the second and third degrees, and a response table was created for the grey relational degrees. As shown in Fig. 6 and Table 7, when the calculations have been performed the "higher the better" normalization sequence approach, the best performance on the $\dot{Q}_{abs}$, $\eta_{rec}$, $\eta_{overall}$, $\dot{m}_{H_2}$ have been provided in the $A_3B_2C_1D_1E_3$ optimum sequence. The optimum array in the test have been determined for $A_3B_2C_1D_1E_3$ sequence as monthly total irradiance average of 143.8 kW h ($A_3$), Wind velocity of 5 m/s ($B_2$), Receiver height of 8 m ($C_1$), Receiver radius of 3 m ($D_1$) and Number of heliostats of 850 ($E_3$), respectively. The useful energy absorbed by the solar receiver ($\dot{Q}_{abs}$), efficiency of the receiver ($\eta_{rec}$), the overall efficiency of the system ($\eta_{overall}$) and hydrogen production ($\dot{m}_{H_2}$) of the optimal combination of parameters ($A_3B_2C_1D_1E_3$) have been computed as 50.2 GW; 64.1%; 22.2% and 122.59 (tons/month), respectively.

The improvement of the grey relation grade (GRG) obtained for $\dot{Q}_{abs}$, $\eta_{rec}$, $\eta_{overall}$, $\dot{m}_{H_2}$ are given in Table 8. The improvement and percentage improvement in GRG for $\dot{Q}_{abs}$, $\eta_{rec}$, $\eta_{overall}$, $\dot{m}_{H_2}$ have been calculated as 0.446 and 86.9 %, as shown in Table 8. These values have been determined to improve the quality characteristics within the reliable range.

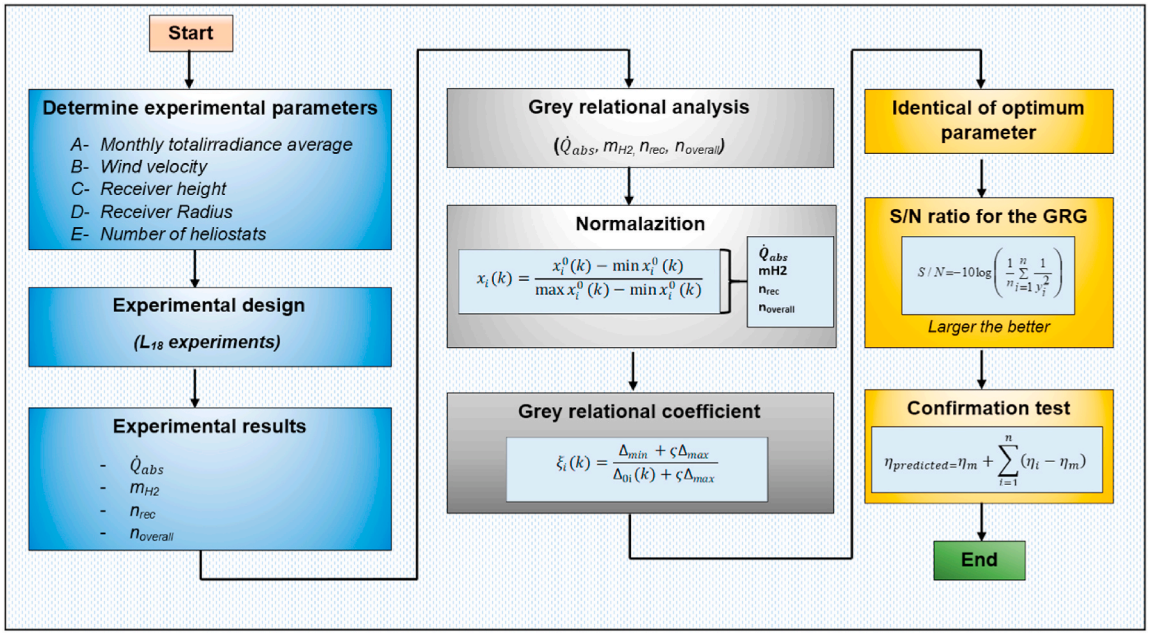



**Fig. 3.** Multi-objective optimization algorithm.

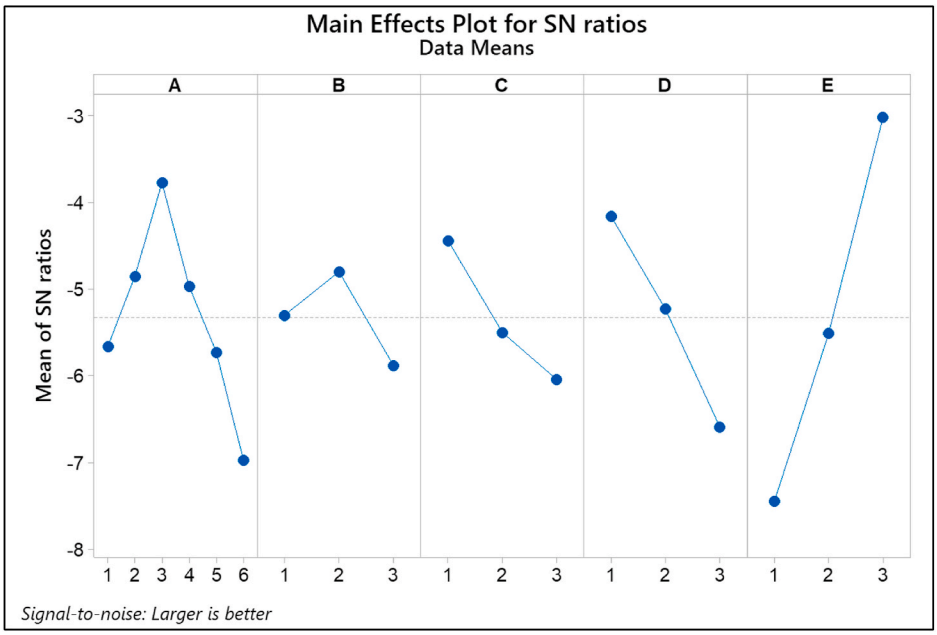



**Fig. 4.** S/N ratios of mean grey relational grades of parameters.

**Table 6**
Results of grey relational analysis.

| Exp. Nu. | Actual results | | | | Normalized values | | | | Coefficients | | | | GRG | S/N | Order |
|---|---|---|---|---|---|---|---|---|---|---|---|---|---|---|---|
| | $\dot{Q}_{abs}$ (MW) | $\dot{m}_{H_2}$ (tons/ month) | $\eta$, rec [−] | $\eta$, overall [-] | $\dot{Q}_{abs}$ (MW) | $\dot{m}_{H_2}$ (tons/ month) | $\eta$, rec [−] | $\eta$, overall [-] | $\dot{Q}_{abs}$ (MW) | $\dot{m}_{H_2}$ (tons/ month) | $\eta$, rec [−] | $\eta$, overall [-] | | | |
| **1** | 17342129 | 42.344 | 0.615 | 0.213 | 0.076 | 0.076 | 0.803 | 0.803 | 0.351 | 0.351 | 0.718 | 0.718 | 0.534 | −5.44236 | 9 |
| **2** | 24474723 | 59.760 | 0.601 | 0.208 | 0.276 | 0.276 | 0.697 | 0.697 | 0.409 | 0.409 | 0.623 | 0.623 | 0.516 | −5.75050 | 11 |
| **3** | 31159512 | 76.082 | 0.585 | 0.202 | 0.464 | 0.464 | 0.578 | 0.578 | 0.483 | 0.483 | 0.542 | 0.542 | 0.513 | −5.80468 | 12 |
| **4** | 35454957 | 86.571 | 0.616 | 0.213 | 0.585 | 0.585 | 0.809 | 0.809 | 0.547 | 0.547 | 0.723 | 0.723 | 0.635 | −3.94606 | 5 |
| **5** | 45083184 | 110.080 | 0.599 | 0.207 | 0.856 | 0.856 | 0.681 | 0.681 | 0.776 | 0.776 | 0.610 | 0.610 | 0.693 | −3.18065 | 4 |
| **6** | 22444127 | 54.802 | 0.563 | 0.195 | 0.219 | 0.219 | 0.413 | 0.413 | 0.390 | 0.390 | 0.460 | 0.460 | 0.425 | −7.42914 | 15 |
| **7** | 48165295 | 117.606 | 0.636 | 0.220 | 0.943 | 0.943 | 0.962 | 0.962 | 0.897 | 0.897 | 0.930 | 0.930 | 0.914 | −0.78525 | 2 |
| **8** | 24565038 | 59.981 | 0.611 | 0.212 | 0.279 | 0.279 | 0.775 | 0.775 | 0.409 | 0.409 | 0.689 | 0.689 | 0.549 | −5.20334 | 6 |
| **9** | 34078454 | 83.210 | 0.589 | 0.204 | 0.546 | 0.546 | 0.605 | 0.605 | 0.524 | 0.524 | 0.559 | 0.559 | 0.542 | −5.32664 | 7 |
| **10** | 32761637 | 79.994 | 0.547 | 0.189 | 0.509 | 0.509 | 0.294 | 0.294 | 0.505 | 0.505 | 0.415 | 0.415 | 0.460 | −6.75180 | 14 |
| **11** | 50206573 | 122.590 | 0.641 | 0.222 | 1.000 | 1.000 | 1.000 | 1.000 | 1.000 | 1.000 | 1.000 | 1.000 | 1.000 | 0.00000 | 1 |
| **12** | 22313318 | 54.483 | 0.538 | 0.186 | 0.216 | 0.216 | 0.227 | 0.227 | 0.389 | 0.389 | 0.393 | 0.393 | 0.391 | −8.15538 | 16 |
| **13** | 18798016 | 45.899 | 0.508 | 0.176 | 0.117 | 0.117 | 0.000 | 0.000 | 0.361 | 0.361 | 0.333 | 0.333 | 0.347 | −9.18356 | 17 |
| **14** | 31771693 | 77.577 | 0.595 | 0.206 | 0.482 | 0.482 | 0.649 | 0.649 | 0.491 | 0.491 | 0.587 | 0.587 | 0.539 | −5.36481 | 8 |
| **15** | 43312983 | 105.758 | 0.620 | 0.214 | 0.806 | 0.806 | 0.839 | 0.839 | 0.721 | 0.721 | 0.756 | 0.756 | 0.738 | −2.63579 | 3 |
| **16** | 31310752 | 76.452 | 0.588 | 0.203 | 0.469 | 0.469 | 0.596 | 0.596 | 0.485 | 0.485 | 0.553 | 0.553 | 0.519 | −5.69551 | 10 |
| **17** | 14648384 | 35.767 | 0.519 | 0.180 | 0.000 | 0.000 | 0.083 | 0.083 | 0.333 | 0.333 | 0.353 | 0.353 | 0.343 | −9.29039 | 18 |
| **18** | 24338929 | 59.429 | 0.597 | 0.207 | 0.273 | 0.273 | 0.669 | 0.669 | 0.407 | 0.407 | 0.602 | 0.602 | 0.505 | −5.94083 | 13 |

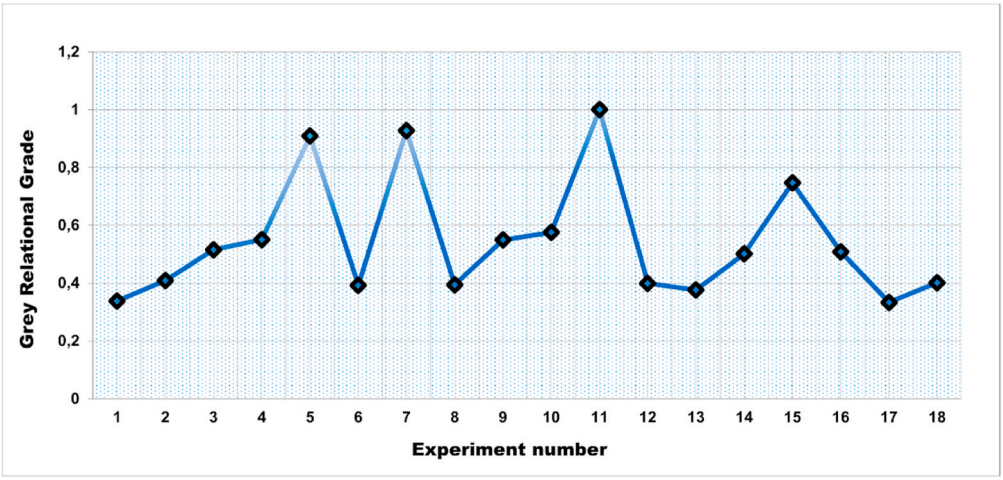



**Fig. 5.** Grey relational grades of tests.

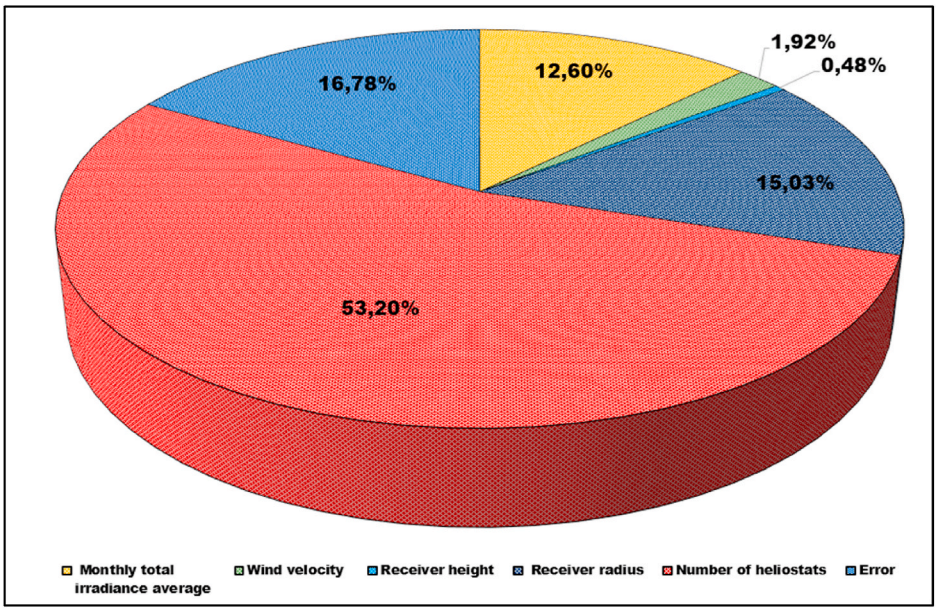



**Fig. 6.** Percent contribution ratios (PCRs) for parameters.

### 4.2. Analysis of variance (ANOVA)

In experimental designs, the effect level of the determined parameters on the results is essential for optimum design. ANOVA analysis method contributes to determining the quantitative effect on the outputs obtained as a result of different parameters. This quantitative effect on the outputs has been calculated as the percent contribution rate (PCR) given in Eq. (31) [40].

$$PCR\% = \left(\frac{SS_A - (V_e).(\upsilon_A)}{SS_T}\right) x100 \tag{31}$$

where $SS_A$ is the sum of squares, $\upsilon_A$ is the degree of freedom, $SS_T$ has represented the total sum of squares, $V_e$ has indicated variance of error.

In addition to PCR, F-test can be used to examine the determined effect parameters. Parameters with higher F values have a more significant impact on the results. The PCR values of each parameter were calculated as given in Table 9 using ANOVA analysis. In the calculations, the effect of the PCR values on the $\dot{Q}_{abs}$, $\eta_{rec}$, $\eta_{overall}$, $\dot{m}_{H_2}$ have been determined to be 12.60 %, 1.92%, 0.48%, 15.03%, and 53.20% for the monthly total irradiance average (A), Wind velocity (B), Receiver height (C), Receiver radius (D) and Number of heliostats (E), respectively. The highest PCR values have been obtained for the number of heliostats, whereas the lowest impact rate was calculated for receiver height. The obtained outputs were verified according to the F-test results, as given in Table 9. According to the ANOVA results, the error rate was calculated as 16.18 % according to the F-test results.

### 4.3. Correlations

Empirical equations provide advantages in terms of time and cost in experimental studies. The result of the desired experiment can be predicted through these equations. In this section, correlations for $\dot{Q}_{abs}$, $\eta_{rec}$, $\eta_{overall}$, $\dot{m}_{H_2}$ are derived. The derived correlations can be used to obtain new parameter results between the determined boundary conditions. Derived empirical equations have been given below:

$$\dot{Q}_{abs} = \text{-}24806071 + 179334A - 901930B - 539228C - 238396D + 55361E \tag{32}$$

$$\dot{m}_{H_2} = \text{-}60.57 + 0.4379A - 2.202B - 1.317C - 0.582D + 0.13518E \tag{33}$$

$$\eta_{rec} = 0.6389 - 0.000019A - 0.0027B - 0.00123C - 0.02757D + 0.000134E \tag{34}$$

$$\eta_{overall} = 0.2211 - 0.000007A - 0.00094B - 0.00042C - 0.00954D + 0.000047E \tag{35}$$

The results obtained were handled in two stages as training and testing for verification tests. In the experiments, the experimental design consists of $L_{18}$, of which 4,9,12, and 16 values have been selected for training and testing. The empirical Eqs. 32–35 obtained for $\dot{Q}_{abs}$, $\eta_{rec}$, $\eta_{overall}$, $\dot{m}_{H_2}$ have been performed for training and testing regression analysis (RA) with 4,9,12, and 16 values. The results were obtained according to actual and empirical Eqs. 32–35 which has testing and training values are given in Table 10. It was observed that the training

**Table 7**
Response table for the GRG (higher the better).

| Level | A | B | C | D | E |
|---|---|---|---|---|---|
| **1** | 0.5209 | 0.5682 | **0.6321** | **0.6528** | 0.4317 |
| **2** | 0.5845 | **0.6068** | 0.5610 | 0.5581 | 0.5326 |
| **3** | **0.6682** | 0.5189 | 0.5008 | 0.4830 | **0.7295** |
| **4** | 0.6169 | | | | |
| **5** | 0.5416 | | | | |
| **6** | 0.4556 | | | | |
| **Delta** | 0.2125 | 0.0879 | 0.1312 | 0.1699 | 0.2977 |
| **Rank** | 2 | 5 | 4 | 3 | 1 |

Bold * values represent the optimal parameter.

**Table 8**
Results of the confirmation test.

| Initial parameters | | Optimum parameters | |
|---|---|---|---|
| | | Prediction | Experiment |
| Level | A1-B1-C2-D2-E2 | A3-B2-C1-D1-E3 | A3-B2-C1-D1-E3 |
| **A** | 143.8 | | 204.4 |
| **B** | 4 | | 5 |
| **C** | 10 | | 8 |
| **D** | 4 | | 3 |
| **E** | 650 | | 850 |
| **GRG** | 0.513 | 1.12054 | 0.959 |

The improvement in GRG = 0.446
The percentage improvement in GRG = 86.9%

**Table 9**
ANOVA results for the GRG.

| Parameter | Degree of freedom | Sum of squares | Mean of squares | F | P | PCR (%) |
|---|---|---|---|---|---|---|
| **A** | 5 | 17.298 | 3.4596 | 4.8 | 0.077 | 12.60 |
| **B** | 2 | 3.53 | 1.765 | 2.45 | 0.202 | 1.92 |
| **C** | 2 | 1.96 | 3.9801 | 5.53 | 0.071 | 0.48 |
| **D** | 2 | 17.786 | 8.8931 | 12.35 | 0.019 | 15.03 |
| **E** | 2 | 59.286 | 29.6431 | 41.16 | 0.002 | 53.20 |
| **Error** | 4 | 2.88 | 0.7201 | | | 16.78 |
| **Total** | 17 | 108.741 | | | | 100 |

and testing results obtained were within acceptable limitations.

The coefficient of determination ($R^2$) and the amount of statistical error (RMSE) were used to determine the deviation rates resulting from the calculation. Calculations for $R^2$ and RMSE are given below [41]:

$$R^2 = 1 - \left( \frac{\sum_{i=1}^{N} (t_i - o_i)^2}{\sum_{i=1}^{N} o_i^2} \right) \tag{36}$$

$$RMSE = \left( \frac{\sum_{i=1}^{N} (t_i - o_i)^2}{\sum_{i=1}^{N} o_i^2} \right)^2 \tag{37}$$

As shown in Table 11, the $R^2$ and RMSE values have been by using Eqs. 36 and 37. The $R^2$ of the training RA for $\dot{Q}_{abs}$, $\eta_{rec}$, $\eta_{overall}$, $\dot{m}_{H_2}$ values have been computed as 0.980493, 0.99608, 0.848267, and 0.848494, respectively, whereas RMSE has been calculated as 0.084039, 0.035065, 0.226414, and 0.226232, respectively. On the other hand, $R^2$ values for testing RA have been computed as 0.976547, 0.990481, 0.771167, and 0.772415, respectively, whereas RMSE has been calculated as 0.095605, 0.059234, 0.273115 and 0.272601. As a result, it has been understood that the $R^2$ and RMSE results obtained and the results obtained according to the actual and empirical equations are within acceptable limits. Also, the comparison of actual, regression training, and testing results for $\dot{Q}_{abs}$, $\eta_{rec}$, $\eta_{overall}$, $\dot{m}_{H_2}$ was plotted in Figs. 7–10, respectively. As shown in Figs. 11–14, the results obtained from derived correlations and actual results were found to be compatible with each other.

Fig. 15 shows monthly hydrogen production ($\dot{m}_{H_2}$) and overall efficiency at optimum design parameters with the Co–Cl thermochemical cycle. As shown in Fig. 15, the highest hydrogen production potential has been calculated as 122.58 tons/month in July, whereas the lowest hydrogen production has been obtained as 29.19 tons/month in December and January. This change in hydrogen production varies seasonally depending on solar radiation. As a result, the multi-objective optimization of the hydrogen production of renewable energy with various thermochemical cycles as the cobalt-chlorine (Co–Cl) thermochemical cycle can be successfully carried out.

The results of the previous study obtained from the literature for different thermochemical process cycles with cobalt are given in Table 12. In Table 12, the energy efficiency of the overall system are compared with the literature. It has been observed that the energy efficiency calculated for the optimal system designed in this study is compatible with the results in the literature.

## 5. Conclusion

This study investigated multi-objective optimization of the hydrogen production of a solar-based cobalt-chlorine (Co–Cl) thermochemical cycle with grey relational analysis (GRA). The main results obtained are as follows.

**Table 10**
Actual and prediction results.

| Exp.*Nu*. | Actual | | | | Regression | | | |
|---|---|---|---|---|---|---|---|---|
| | $\dot{Q}_{abs}$ (MW) | $\dot{m}_{H_2}$ (tons/month) | $\eta$, rec | $\eta$, overall | $\dot{Q}_{abs}$ (MW) | $\dot{m}_{H_2}$ (tons/month) | $\eta$, rec | $\eta$, overall |
| **1.** | 17342129 | 42.344 | 0.615 | 0.213 | 28749557 | 41.984 | 0.593 | 0.205 |
| **2.** | 24474723 | 59.760 | 0.601 | 0.208 | 38638610 | 59.078 | 0.587 | 0.203 |
| **3.** | 31159512 | 76.082 | 0.585 | 0.202 | 48527663 | 76.172 | 0.581 | 0.202 |
| [a]**4.** | 35454957 | 86.571 | 0.616 | 0.213 | 58531168 | 107.647 | 0.585 | 0.203 |
| **5.** | 45083184 | 110.080 | 0.599 | 0.207 | 40421479 | 56.377 | 0.582 | 0.201 |
| **6.** | 22444127 | 54.802 | 0.563 | 0.195 | 60980639 | 116.606 | 0.643 | 0.223 |
| **7.** | 48165295 | 117.606 | 0.636 | 0.220 | 38575292 | 54.848 | 0.557 | 0.193 |
| **8.** | 24565038 | 59.981 | 0.611 | 0.212 | 48540996 | 82.159 | 0.559 | 0.194 |
| [a]**9.** | 34078454 | 83.210 | 0.589 | 0.204 | 62885853 | 122.353 | 0.643 | 0.223 |
| **10.** | 32761637 | 79.994 | 0.547 | 0.189 | 33800941 | 50.243 | 0.535 | 0.185 |
| **11.** | 50206573 | 122.590 | 0.641 | 0.222 | 47985652 | 77.825 | 0.611 | 0.212 |
| [a]**12.** | 22313318 | 54.483 | 0.538 | 0.186 | 58034851 | 107.531 | 0.613 | 0.212 |
| **13.** | 18798016 | 45.899 | 0.508 | 0.176 | 26513054 | 33.545 | 0.535 | 0.185 |
| **14.** | 31771693 | 77.577 | 0.595 | 0.206 | 40697765 | 61.127 | 0.612 | 0.212 |
| **15.** | 43312983 | 105.758 | 0.620 | 0.214 | 48642115 | 90.553 | 0.591 | 0.205 |
| [a]**16.** | 31310752 | 76.452 | 0.588 | 0.203 | 48624491 | 84.554 | 0.558 | 0.193 |
| **17.** | 14648384 | 35.767 | 0.519 | 0.180 | 40480506 | 60.595 | 0.556 | 0.193 |
| **18.** | 24338929 | 59.429 | 0.597 | 0.207 | 48758255 | 82.691 | 0.614 | 0.213 |
| [a]**Optimum** | 48745071 | 119.021 | 0.644 | 0.223 | 62885853 | 122.353 | 0.643 | 0.223 |
| [a]**Initial** | 24636173 | 60.154 | 0.605 | 0.209 | 36614951 | 57.115 | 0.562 | 0.195 |

[a] Excluded for testing.

**Table 11**
Statistical results of the $\dot{Q}_{abs}$ and $\dot{m}_{H_2}$.

| Regression | $\dot{Q}_{abs}$ (MW) | | $\dot{m}_{H_2}$ (tons/month) | | $\eta$, rec | | $\eta$, overall | |
|---|---|---|---|---|---|---|---|---|
| | RMSE | $R^2$ | RMSE | $R^2$ | RMSE | $R^2$ | RMSE | $R^2$ |
| **Training** | 0.084039 | 0.980493 | 0.035065 | 0.99608 | 0.226414 | 0.848267 | 0.226232 | 0.848494 |
| **Testing** | 0.095605 | 0.976547 | 0.059234 | 0.990481 | 0.273115 | 0.771167 | 0.272601 | 0.772415 |

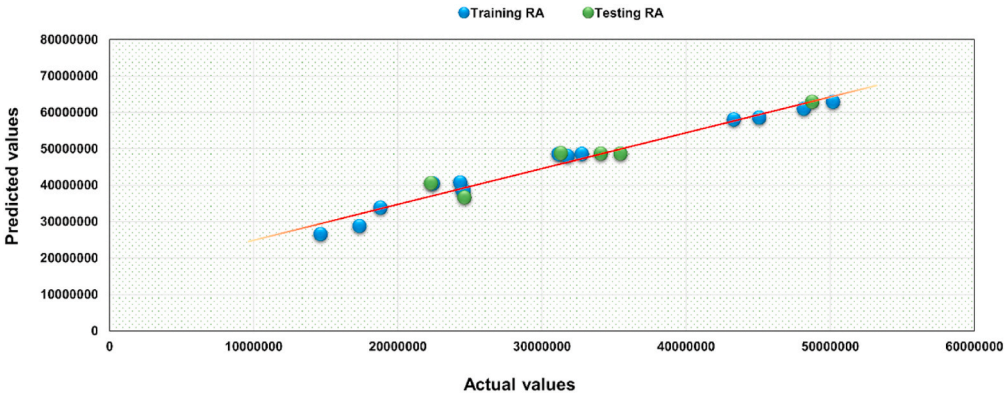



**Fig. 7.** Comparison of $\dot{Q}_{abs}$ actual results with RA results.




**Fig. 8.** Comparison of $\dot{m}_{H_2}$ actual results with RA results.

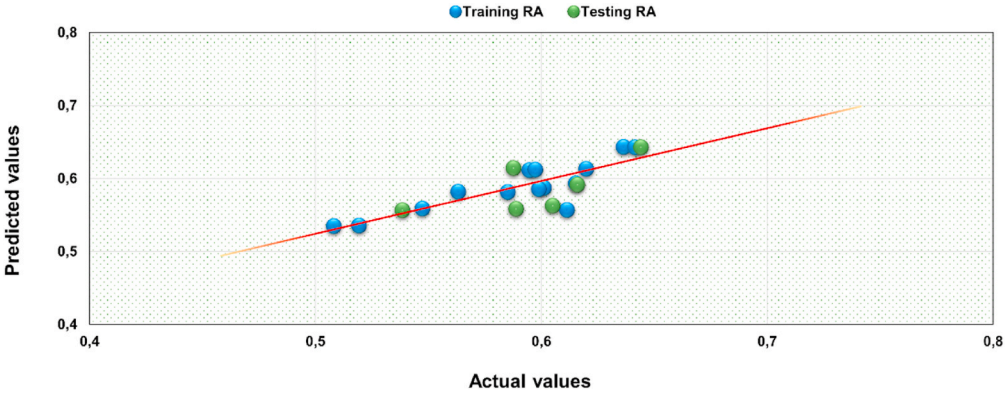



**Fig. 9.** Comparison of $\eta_{rec}$ [−] actual results with RA results.

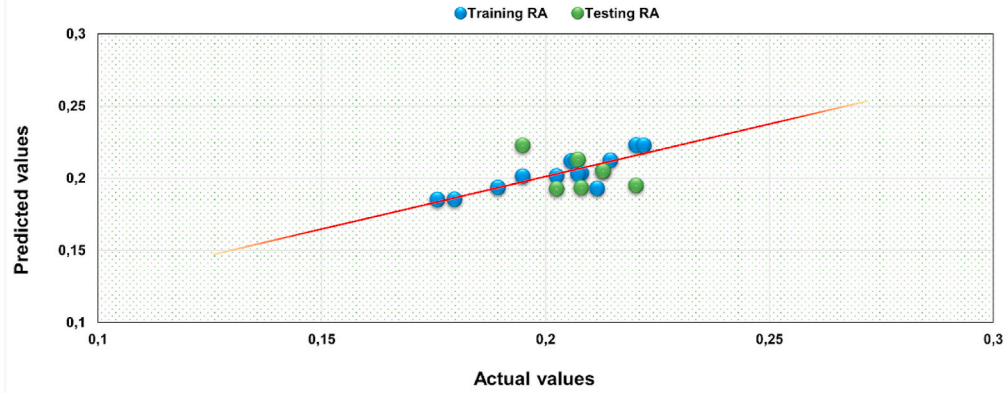



**Fig. 10.** Comparison of $\eta_{overall}$ [−] actual results with RA results.

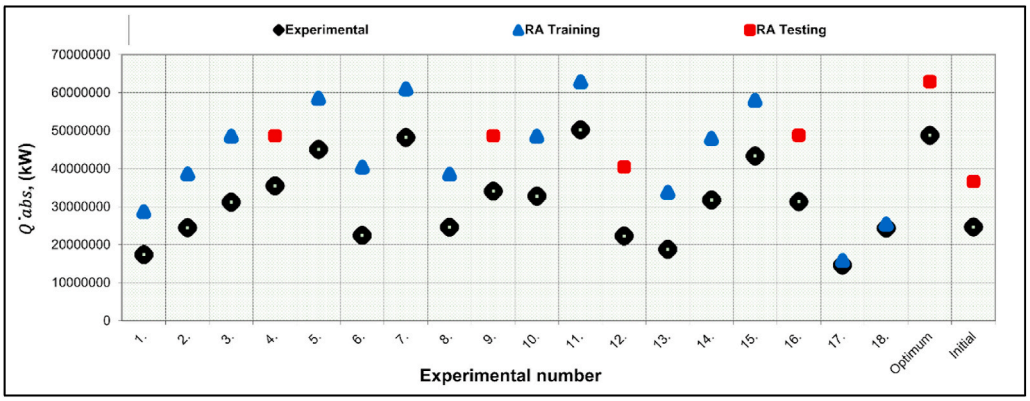



**Fig. 11.** Comparison of actual and predicted results for $\dot{Q}_{abs}$.

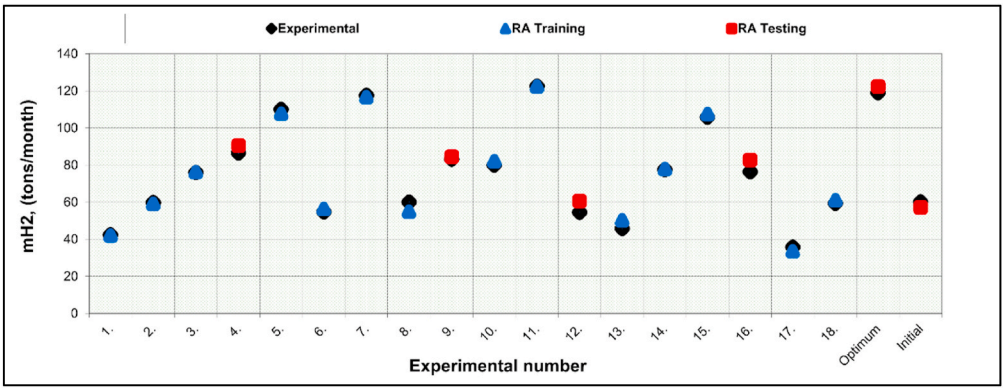



**Fig. 12.** Comparison of actual and predicted results for $\dot{m}_{H_2}$.

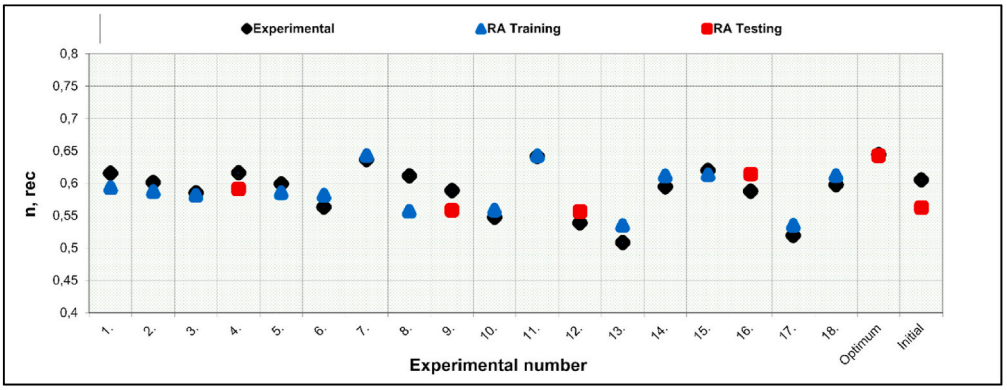



**Fig. 13.** Comparison of actual and predicted results for $\eta_{rec}$ [−].

- ✓ The optimum levels for $\dot{Q}_{abs}$, $\eta_{rec}$, $\eta_{overall}$, $\dot{m}_{H_2}$ have been provided in the $A_3B_2C_1D_1E_3$ optimum sequence. The optimum array in the test has been determined as monthly total irradiance average 143.8 kW h ($A_3$), Wind velocity ($B_2$) = 5 m/s, Receiver height ($C_1$) = 8 *m*, Receiver radius ($D_1$) = 3 *m* and Number of heliostats ($E_3$) = 850, respectively.
- ✓ The contribution levels (PCR) of the parameters for the $\dot{Q}_{abs}$, $\eta_{rec}$, $\eta_{overall}$, $\dot{m}_{H_2}$ are determined as 12,6 %, 1,92 %, 0,48 %, 15,03 %, and 53,20 %, respectively, for the $A_3B_2C_1D_1E_3$ optimum sequence.
- ✓ The overall efficiency of the system ($\eta_{overall}$) and hydrogen production ($\dot{m}_{H_2}$) of the $A_3B_2C_1D_1E_3$ have been found as 22,2% and 122.59 (tons/month), respectively.
- ✓ $R^2$ on the $\dot{Q}_{abs}$, $\eta_{rec}$, $\eta_{overall}$, $\dot{m}_{H_2}$ values have been obtained in the range of 0.99608 and 0.771167 for both training and testing, whereas RMSE has been calculated as between 0.273115 and 0.035065, respectively.
- ✓ Empirical equations derived with RA revealed good agreement between predicted and actual results.
- ✓ The monthly hydrogen production ($\dot{m}_{H_2}$) in optimum design parameters have been computed in the range of 30 and 125 tons/month.
- ✓ The GRA method is an efficient and effective tool to optimize the hydrogen production analysis for renewable energy sources.

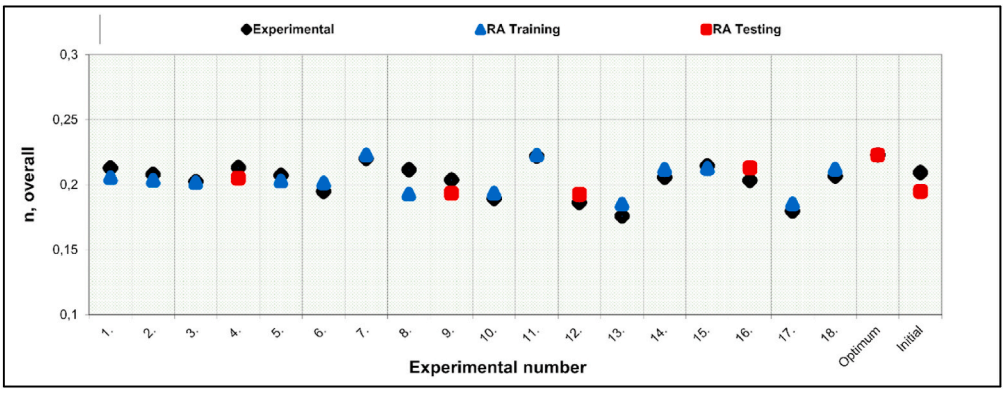



**Fig. 14.** Comparison of actual and predicted results for $\eta_{overall}$ [−].

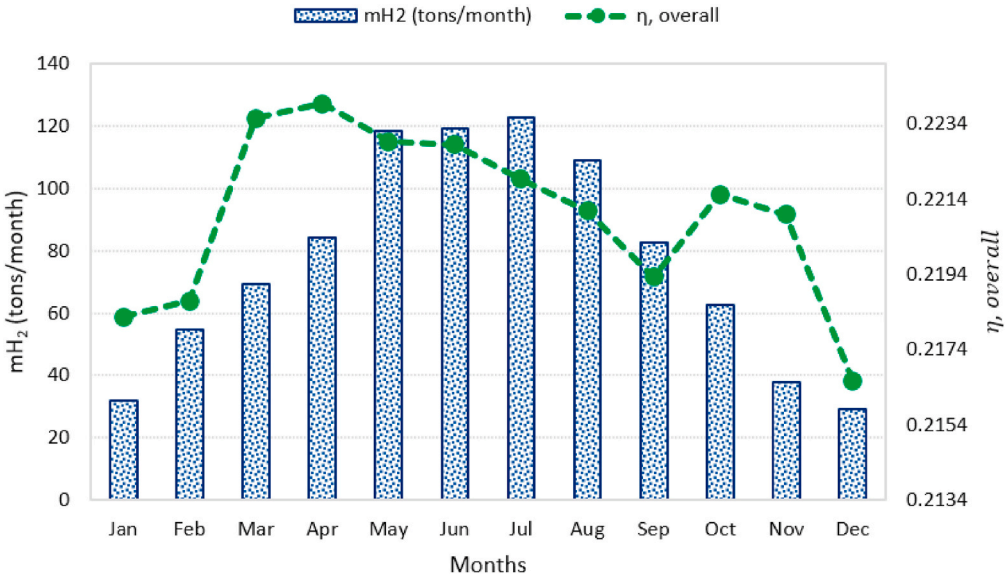



**Fig. 15.** Monthly hydrogen fuel production and overall efficiency at optimum design parameters.

**Table 12**
Comparative of the overall energy efficiencies of hydrogen production cycles.

| Cycle | Energy Efficiency | Ref. |
|---|---|---|
| Four step Co–Cl | 22.2% | Present work |
| Three step Mg–Cl, | 23–25% | [11] |
| Three step $H_2SO_4$ | 24–25% | |
| Four Step UT-3 | 24 % | |
| Four step Heavy element halide cycle | 26.1% | [42] |
| Four Step Cu–Cl | 27.4 % | [43] |
| Three Step Mg–Cl | 18.8 % | [44] |
| Three step Sodium Hydroxide (NaOH) | 11% | [45] |

## CRediT authorship contribution statement

**Ramazan Çakıroğlu:** Methodology, Software, Validation, Writing – original draft, Writing – review & editing. **Oğuz Kaan Çinici:** Resources, Writing – review & editing. **Şulenur Asal:** Data curation, Investigation, Resources, Validation. **Adem Acır:** Resources, Supervision, Validation, Writing – original draft, Writing – review & editing.

## Declaration of competing interest

I declare this paper has not been published previously, it is not under consideration for publication elsewhere, and if accepted it will not be published elsewhere in substantially the same form, in English or in any other language, without the written consent of the publisher. There is no conflict of interest in my article.

## Nomenclature

| | |
|---|---|
| A | Area ($m^2$), monthly total irradiance average (kWh) |
| B | wind velocity (m/s) |
| C | concentration ratio, receiver height (m) |
| D | receiver radius (m) |
| E | number of heliostats |
| $F_r$ | view factor |
| g | gravity ($m/s^2$) |
| H | heat of fusion (kJ/kg) |
| h | heat conductivity coefficient (W/mK), specific enthalpy (kJ/kg) |
| $h_0$ | reference enthalpy (kJ/kg) |
| HHV | higher heating value (MJ/kg) |
| I | solar flux ($W/m^2$) |
| $\dot{m}$ | mass flow rate (kg/s) |
| *Nu* | Nusselt number |
| k | heat transfer coefficient ($W/m^2K$) |
| $P_0$ | reference pressure (bar) |
| q | energy value (MJ/kg) |
| Pr | Prandtl number |
| $R^2$ | coefficient of determination |
| Re | Reynolds number |
| $\dot{Q}$ | heat transfer rate (kW) |
| T | temperature (K) |
| $T_0$ | reference temperature (K) |
| V | speed (m/s), variance |
| W | width (m) |
| $\dot{W}$ | work rate or electric power (kW) |
| Z | height (m) |

*Greek Letters*

| | |
|---|---|
| Δ | difference |
| $\delta$ | thickness |
| $\varepsilon$ | emmisivity |
| η | energy efficiency |
| λ | conductivity |
| $\rho$ | reflectivity |
| $\upsilon$ | degree of freedom |
| $\varphi$ | fraction |

*Subscripts*

| | |
|---|---|
| a | air |
| abs | absorption |
| ape | aperture |
| avg | average |
| cond | conduction |
| conv | convection |
| e | error |
| *f* | formation |
| *fc* | forced convection |
| field | heliostat field |
| g | gas |
| h | heliostat |
| in | inlet |
| insu | insulation |
| *nc* | natural convection |
| rad | radiation |
| rec | receiver |
| ref | reflection |
| out | outlet |
| s | solid |
| surf | surface |
| tot | total |

*Abbreviations*

| | |
|---|---|
| ANOVA | Analysis of variance |
| GRA | Grey relational analysis |
| GRG | Grey relational grade |
| RA | Regression Analysis |
| LIFE | Laser Inertial Fission-Fusion Engine |
| PCM | Phase change materials |
| PCR | Percent contribution rate |
| PEM | Proton exchange membrane |
| PV | Photovoltaic |
| RMSE | Root-mean-square error |
| RSM | Response surface method |
| SS | Sum of squares |
| TEG | Thermoelectric generator |
| TES | Thermal energy storage |

## References


[1] Veziroğlu TN, Şahin S. 21st Century's energy: hydrogen energy system. Energy Convers Manag 2008;49(7):1820–31.
[2] Paparao J, Murugan S. Oxy-hydrogen gas as an alternative fuel for heat and power generation applications - a review Hydrogen enriched Compressed Natural Gas. Int J Hydrogen Energy 2021;46(76):37705–35.
[3] Gambini M, Guarnaccia F, Manno M, Vellini M. Ragone plots of material-based hydrogen storage systems. J Energy Storage 2024;76:109815.
[4] Li X, Sun X, Song Q, Yang Z, Wang H. A critical review on integrated system design of solar thermochemical water-splitting cycle for hydrogen production Organic Rankine cycle. Int J Hydrogen Energy 2022;47(79):33619–42.
[5] Demir ME, Dincer I. Development of a hybrid solar thermal system with TEG and PEM electrolyzer for hydrogen and power production. Int J Hydrogen Energy 2017;42(51). 30044–300456.-14.
[6] Behzadi A, Gholamian E, Alirahmi SM, Nourozi B, Sadrizadeh S. A comparative evaluation of alternative optimization strategies for a novel heliostat-driven hydrogen production/injection system coupled with a vanadium chlorine cycle. Energy Convers Manag 2022;267. 115878.-15.
[7] Ratlamwala TAH, Dincer I, Aydin M. Energy and exergy analyses and optimization study of an integrated solar heliostat field system for hydrogen production. Int J Hydrogen Energy 2012;37(24):18704–12. 16.
[8] Musharavati F, Khanmohammadi S, Mansir IB. Design, exergy analysis, and optimization of a hydrogen generation/storage energy system with solar heliostat fields and absorption-ejector refrigeration system. Int J Hydrogen Energy 2022;47(62). 25945–259463.-17.
[9] Alirahmi SM, Razmi AR, Arabkoohsar A. Comprehensive assessment and multi-objective optimization of a green concept based on a combination of hydrogen and compressed air energy storage (CAES) systems. Renew Sustain Energy Rev 2021;142. 110850.-18.
[10] Izadi A, Ahmadi P, Bashiri Mousavi S, Fakhari I. A comparative optimization of a trigeneration system with an innovative integration of solar Heliostat towers and Hydrogen production unit. Sustain Energy Technol Assessments 2021;47. 101522.-19.
[11] Ozdemir A, Genç G. A comprehensive comparative energy and exergy analysis in solar based hydrogen production systems. Int J Hydrogen Energy 2022;47(24):12189–203. 20.
[12] El-Emam RS, Dincer I. Development and assessment of a novel solar heliostat-based multigeneration system. Int J Hydrogen Energy 2018;43(5). 2610-2620.-21.
[13] Hai T, Dhahad HA, Attia E, Zakaria Z, et al. Design, modeling and multi-objective techno-economic optimization of an integrated supercritical Brayton cycle with solar power tower for efficient hydrogen production. Sustain Energy Technol Assessments 2022;53. 102599.-22.
[14] Canavesio C, Nassini D, Nassini HE, Bohé AE. Study on an original cobalt-chlorine thermochemical cycle for nuclear hydrogen production. Int J Hydrogen Energy 2020;45(49):26090–103.
[15] Asal Ş, Acır A. A study on nuclear hydrogen production using a novel approach cobalt-chlorine thermochemical cycle in a laser driver fission fusion blanket for various molten salt fuels. Prog Nucl Energy 2022;153(September):104443.
[16] Oruç O, Dincer İ. Exergy analysis of Cobalt–Chlorine thermochemical hydrogen production cycle: a kinetic approach. Int J Hydrogen Energy 2022;47(73):31165–73.
[17] Asal Ş, Acır A. Evaluation and comparison of hydrogen production potential of the LIFE fusion reactor by using copper–chlorine (Cu–Cl), cobalt–chlorine (Co–Cl) and sulfur–iodine (S–I) cycles. Int J Hydrogen Energy 2023;48(60):22791–805.
[18] Acır A, Canlı ME, Ata İ, Çakıroğlu R. Parametric optimization of energy and exergy analyses of a novel solar air heater with grey relational analysis. Appl Therm Eng 2017;122. 330-338-9.
[19] Çinici OK, Canlı ME, Çakıroğlu R, Acır A. Optimization of melting time of solar thermal energy storage unit containing spring type heat transfer enhancer by Taguchi based grey relational analysis, vol. 47; 2022.
[20] "Internet: https://www.mgm.gov.tr/veridegerlendirme/il-ve-ilceler-istatistik.aspx?k=parametrelerinTurkiyeAnalizi.".
[21] Shahin MS, Orhan MF, Uygul F. Thermodynamic analysis of parabolic trough and heliostat field solar collectors integrated with a Rankine cycle for cogeneration of electricity and heat. Sol Energy 2016;136:183–96.
[22] Mostafavi Tehrani SS, Taylor RA. Off-design simulation and performance of molten salt cavity receivers in solar tower plants under realistic operational modes and control strategies. Appl Energy 2016;179:698–715.
[23] Pourrahmani H, Moghimi M. Exergoeconomic analysis and multi-objective optimization of a novel continuous solar-driven hydrogen production system assisted by phase change material thermal storage system. Energy 2019;189:116170.
[24] Ratlamwala TAH, Dincer I. Performance assessment of solar-based integrated Cu-Cl systems for hydrogen production. Sol Energy 2013;95:345–56.
[25] Hu Y, Xu Z, Zhou C, Du J, Yao Y. Design and performance analysis of a multi-reflection heliostat field in solar power tower system. Renew Energy 2020;160:498–512.
[26] Xu C, Wang Z, Li X, Sun F. Energy and exergy analysis of solar power tower plants. Appl Therm Eng 2011;31(17–18):3904–13.
[27] Balta MT, Dincer I, Hepbasli A. Performance assessment of solar-driven integrated Mg-Cl cycle for hydrogen production. Int J Hydrogen Energy 2014;39(35):20652–61.
[28] Li X, Kong W, Wang Z, Chang C, Bai F. Thermal model and thermodynamic performance of molten salt cavity receiver. Renew Energy 2010;35(5):981–8.
[29] Falcone PK. A handbook for solar central receiver design (No. SAND-86-8009). Livermore, CA (United States): Sandia National Lab.(SNL-CA); 1986.
[30] Siebers DL, Kraabel JS. Estimating convective energy losses from solar central receivers (No. SAND-84-8717). Sandia National Lab. Livermore, CA (United States): SNL-CA); 1984.
[31] Rizvi AA, Danish SN, El-Leathy A, Al-Ansary H, Yang D. A review and classification of layouts and optimization techniques used in design of heliostat fields in solar central receiver systems. Sol Energy 2021;218:296–311.
[32] Ahmadi A, Ehyaei M, Jamali D, Despotovic M, Esmaeilion F, Abdalisousan A, Hani EB. Energy, exergy, and economic analyses of integration of heliostat solar receiver to gas and air bottom cycles. J Clean Prod 2021;280:124322.
[33] Asal Ş, Acır A. A study on nuclear hydrogen production using a novel approach cobalt-chlorine thermochemical cycle in a laser driver fission fusion blanket for various molten salt fuels. Prog Nucl Energy 2022;153(September):104443.
[34] Asal Ş, Acır A. Utilization of the Cu–Cl thermochemical cycle for hydrogen production using a laser driver thorium molten salts. Int J Hydrogen Energy 2021;6(61):31133–42.
[35] Cengel Y, Boles M. In: Thermodynamics an engineering approach; 2012.
[36] NIST chemistry WebBook. 2018. http://webbook.nist.gov/chemistry/.
[37] Zou L, Shen Q, Yang G, Li S, Huang N. Improved hydrogen production efficiency of a Photovoltaic-Electrolysis system with P&O Algorithm: a case study. Chem Phys Lett 2023;832:140891.
[38] Deng J. Introduction to grey system theory. J Grey Syst 1989;1:1–24.
[39] Ye W, Wang W, Zhu J, Liu Y. Optimizing design of a free piston Stirling engine using response surface methodology and grey relation analysis. Case Stud Therm Eng 2024;54:103981.
[40] Çakıroğlu R, Acır A. Optimization of cutting parameters on drill bit temperature in drilling by Taguchi method. Measurement 2013;46(9):3525–31.
[41] Acır A. Application of artificial neural network to exergy performance analysis of coal fired thermal power plant. Int J Exergy 2013;12(3):362–37955.
[42] Sorgulu F, Dinçer İ. A solar energy driven thermochemical cycle based integrated system for hydrogen production. Energy 2023;269:126834.
[43] Temiz M, Dincer İ. Concentrated solar driven thermochemical hydrogen production plant with thermal energy storage and geothermal systems. Energy 2021;219:119554.
[44] Özcan H, Dinçer İ. Energy and exergy analyses of a solar driven Mg-Cl hybrid thermochemical cycle for co-production of power and hydrogen. Int J Hydrogen Energy 2014;39(28):15330–41. 23.
[45] Oruc Onur, Dincer İ. Analysis and assessment of a new solar assisted sodium hydroxide thermochemical hydrogen production cycle. Energy Convers Manag 2021;237:114139.